241 (2024) 213166

Contents lists available at ScienceDirect

Geoenergy Science and Engineering

journal homepage: www.sciencedirect.com/journal/geoenergy-science-and-engineering

Thermo-poroelastic AVO modeling of Olkaria geothermal reservoirs

Yifan Cheng [a,b], Li-Yun Fu [a,b,c,*], Wanting Hou [a,b], José M. Carcione [d], Wubing Deng [a,c], Zhiwei Wang [e]

[a] State Key Laboratory of Deep Oil and Gas, China University of Petroleum (East China), Qingdao 266580, China
[b] School of Geosciences, China University of Petroleum (East China), Qingdao 266580, China
[c] Laboratory for Marine Mineral Resources, Qingdao National Laboratory for Marine Science and Technology, Qingdao 266071, China
[d] Nazional Institute of Oceanography and Geophysics (OGS), Trieste 34010, Italy
[e] College of Underwater Acoustic Engineering, Harbin Engineering University, China

ARTICLE INFO

Keywords:
Geothermal reservoir
AVO response
Thermo-poroelastic AVO method
Wave propagation
Seismic monitoring

ABSTRACT

Seismic AVO has a significant potential for fluid identification in time-lapse monitoring of the cyclic recovery of geothermal reservoirs. With this goal, we develop an AVO method based on the reflection and transmission (R/T) of elastic waves at an interface between two fluid-saturated thermo-poroelastic media. The method is applied to the Olkaria geothermal reservoir modeling in Kenya. This system is characteristic of a natural cyclic recovery, where cyclic meteoric water undergoes complex phase transition and thermo-hydro-mechanical coupling process. Conceptual models are built based on petrophysical and thermophysical properties of trachyte thermal reservoirs, and the fluid properties under different temperature conditions have been considered. A plane-wave analysis illustrates the effects of thermal conductivity, specific heat, and porosity on velocity dispersion and attenuation of the fast-P, Biot P, and thermal P waves. AVO modeling by P-wave incidence is conducted to investigate the effects of temperature, porosity, and fluid type on the R/T coefficients. For trachyte reservoirs with a temperature less than 500 °C, limited changes in the thermophysical properties have negligible effects on wave propagation, whereas significant effects are due to temperature, porosity, and fluid type. Synthetic seismogram also indicates that the thermo-poroelastic effect noticeable changes the seismic responses compared with the traditional elastic and thermoelastic models. The thermo-poroelastic AVO method proposed in this paper reveals the variation of R/T coefficients of geothermal reservoirs under different conditions. The results can be used as a precursor to geothermal reservoir monitoring, fluid leakage or short circuits.

1. Introduction

Geothermal fields provide a clean and low-carbon renewable energy with large storage capacity (Wang et al., 2018). The intense tectonic activity in the East African Rift Valley led to the upwelling of deep heat flows, creating a series of high-temperature geothermal zones. The Kenya Rift, located in the eastern part, forms many volcanic geothermal systems with development potential (Rop et al., 2013). The Olkaria geothermal field is considered the most promising, with an installed geothermal capacity of 1110 MW in 2020. To meet the growing demand for electricity and mitigate climate change, more careful development of geothermal fields is required. Enhanced geothermal system (EGS) has been widely used to extract heat by creating an artificial liquid circulation system (e.g., water or CO_2) through fracturing techniques to enhance the permeability of geothermal reservoir (AbuAisha et al., 2016; Pandey et al., 2018). The Olkaria geothermal system is a natural EGS (West, 2009), where meteoric water percolates down along the major fractures and partly from infiltration. The groundwater flows laterally due to pressure difference and recharges into the geothermal system, where it is heated and then rises in the upflow zones. This upward steam and water mixture condenses below the cap rock and sinks again in a kind of convective cycle. EGSs involve complex thermal-liquid-solid coupling processes (Breede et al., 2013; Liu et al., 2018; Cui and Wong, 2021), where geophysical exploration plays a crucial role. Many researches show that comprehensive geophysical data can be used to characterize geothermal reservoirs (Vidal et al., 2017; Rathnaweera et al., 2020) and reduce the risk of exploration (Guitton, 2020). Particularly, the elastic seismic amplitude variation with offset and azimuth (AVOA) model that couples fluid-flow and geomechanics can predict seismic anisotropies and microseismicity in

* Corresponding author. State Key Laboratory of Deep Oil and Gas, China University of Petroleum (East China), Qingdao 266580, China.
E-mail address: lfu@upc.edu.cn (L.-Y. Fu).

https://doi.org/10.1016/j.geoen.2024.213166
Received 23 December 2023; Received in revised form 14 April 2024; Accepted 22 July 2024
Available online 23 July 2024

the production process (Angus et al., 2015).

In recent decades, numerous geophysical surveys have taken place in the Olkaria geothermal field. The strong attenuation of S-waves indicates the presence of several molten magma chambers in the Olkaria area at 6 km depth, which are considered to be the main source of heat (Simiyu and Keller, 2000). Gravity data and aeromagnetic data show high temperature and high-density intrusions in the same locations while delineating the distribution of major fracture zones (Simiyu and Keller, 2001). Transient electromagnetic and magnetotelluric measurements identify important thermal reservoirs and heat flow channels in the Olkaria geothermal field (Anastasia, 2014). A comprehensive analysis of these geophysical studies in conjunction with temperature-pressure test data from boreholes led to a conceptual model of the Olkaria geothermal system (Rop et al., 2018; Shi et al., 2021). The conceptual model describes the characteristics of the geothermal field, but the limited data resolution prevents an accurate description of the state of the thermal reservoir, such as temperature gradients, fracture networks and petrophysical properties.

Therefore, real-time (or near real-time) seismic monitoring is critical for evaluating the operational efficiency and fluid path of geothermal fields (Guo and Thurber, 2022). Particularly, high-resolution 3D seismic imaging (Salaun et al., 2020) can reveal the distribution of deep thermal reservoir fracture networks. Numerous petrophysical experimental have studied the sensitivity of seismic characteristics to temperature variations (Batzle and Wang, 1992; Qi et al., 2021; Yang et al., 2021). Poletto et al. (2018) present a brittle-ductile behavior theory and sensitivity analysis based on the Burgers model, integrated with a modified Gassmann model for fluid saturated porous rocks, squirt-flow loss, as well as pressure effects. Wei et al. (2021) performed a joint inversion of temperature and pressure in the subsurface by linking temperature, pressure and porosity to P-wave impedance, VP/VS ratios and seismic attenuation via 3D rock physics templates. These studies demonstrate the potential of using reflection seismic data for detailed characterization of geothermal reservoirs. The effects of pressure and temperature on the elastic properties of geothermal rocks are mainly related to seismic reflection characteristics, the physics of which is relevant to the behavior of reflection and transmission (R/T) of elastic waves.

Amplitude variation with offset (AVO) (Fawad et al., 2020) is one method used to estimate the properties of reservoirs. Conventional AVO methods cannot be directly applied to geothermal reservoirs because they do not consider temperature effects on both the rock and fluid properties. For this purpose, we use the thermo-poroelastic theory to calculate the R/T coefficients for elastic waves based on the Lord-Shulman (LS) approach (Lord and Shulman, 1967), that has been applied to investigate the effect of the thermophysical properties in non-porous media on wave propagation (Carcione et al., 2018; Wang et al., 2020; Hou et al., 2021). The theory predicts the typical P and S waves, as well as slow-P diffusive wave (thermal mode). These two P-wave modes are similar to the classical porelastic model, with the difference that the slow-P wave is induced by thermal flux (not to fluid flow as in poroelasticity). The thermal mode is diffusive at low frequencies. The R/T phenomena of thermoelastic waves have been extensively studied. For instance, a comprehensive review (Hou et al., 2022a) identifies existing mistakes and flaws in previous studies, especially when the presence of inhomogeneous plane waves is neglected. Based on the R/T of waves incident at a preheated interface and their propagation in multilayered thermal media (Hou et al., 2022b), Hou et al. (2023) extend the conventional AVO method to thermoelastic media for seismic exploration of superdeep high-temperature oil/gas resources.

The LS theory has been extended to the case of porous media (i.e., the so-called thermo-poroelasticity) by incorporating Biot poroelasticity to couple elastic deformations with temperature (Noda, 1990; Carcione et al., 2019; Baldonedo et al., 2020). The theory predicts the presence of both Biot and thermal slow P waves besides the classical P and S waves. Fourier pseudospectral numerical simulations have demonstrated (Carcione et al., 2019) that the conversion from fast waves to thermal modes leads to mesoscopic energy attenuation. Wei et al. (2020) develop a frequency-domain Green's function as displacement-temperature solutions of thermo-poroelasticity to study the effect of fluid viscosities and thermophysical properties. Based on the Biot-Rayleigh double--porosity theory (Ba et al., 2011), Li et al. (2022) extend the LS thermo-poroelasticity to the case of double porosity system by considering the local heat/fluid flows in both types of pores. The double-porosity thermo-poroelasticity theory has been used to develop a thermo-hydro-mechanical model (Li et al., 2023) for the evaluation of the seismic properties of geothermal reservoirs in the cyclic recovery of fractured-vuggy geothermal reservoirs. Regarding the R/T phenomena of thermo-poroelastic waves, Wang et al. (2021) investigate the reflection of inhomogeneous plane waves at a free surface. Hou et al. (2022a) further investigated the R/T of inhomogeneous plane waves at the interface between two fluid-saturated thermo-poroelastic media. In this work, we investigate AVO, based on the R/T coefficients. The AVO modeling developed in this work is applied to the Olkaria geothermal reservoir modeling. The results have positive significance to enable time-lapse reflection seismic monitoring for EGSs.

We first introduce the theory of thermo-poroelasticity and then formulate the AVO method. The characteristics of Olkaria geothermal reservoir in Kenya are considered based on previous study (Fu, 2019). We conduct a plane-wave analysis to investigate the effect of the thermal properties on wave velocity and attenuation. Finally, the AVO response is investigated for the effect of temperatures, porosities and fluids. We demonstrate that the velocity dispersion and angle-dependent amplitude due to thermal effects with rock skeletons and pore fluids offer an important indicator that could be potentially used to monitor the operation efficiency of EGSs.

2. Thermo-poroelasticity theory and AVO method

2.1. Wave propagation theory

The LS thermo-poroelastic theory describes wave losses caused by fluid and heat flows due to the presence of the Biot and thermal slow P waves. The theory can be used to accurately describe wave propagation in geothermal reservoirs, which is the basis for the study of reflection and transmission coefficients. We define the thermo-poroelastic media in which γ is the thermal conductivity, C_e is the specific heat, $\rho = (1-\phi)\rho_s + \phi\rho_f$ is the composite density with ρ_s and ρ_f the grain and fluid densities, bulk porosity ϕ, relaxation time τ, and T is the increment of temperature over a reference T_0. The displacement components u_i and w_i represent the solid and fluid phases, respectively. Thermal modulus $\beta = \beta_s + \alpha\beta_f$, with β_s and β_f represent the thermal stress coefficients of the solid and fluid phases. The dot above the variables indicates the time differentiation.

The constitutive relations of the thermo-poroelasticity theory are given in the Appendix. The wave equations for displacement components and temperature fluctuations in an isotropic porous medium saturated with viscous fluid from Eq. (A.3) are (Carcione et al., 2019)

$$\begin{cases} \rho\ddot{u}_i + \rho_f\ddot{w}_i = \left(\lambda+\mu+\alpha^2 M\right)u_{j,ij} + \mu u_{i,jj} + \alpha M w_{j,ij} - \beta T_{,i} \\ \rho_f\ddot{u}_i + q\ddot{w}_i + r\dot{w}_i = M\left(\alpha u_{j,ij} + w_{j,ij}\right) - \dfrac{\beta_f}{\phi}T_{,i} \\ \gamma T_{,ii} = \rho C_e\left(\dot{T} + \tau\ddot{T}\right) + \beta T_0\left[\dot{u}_{i,i} + \dot{w}_{i,i} + \tau\left(\ddot{u}_{i,i} + \ddot{w}_{i,i}\right)\right] \end{cases}, \tag{1}$$

where $r = \eta/\kappa$, with η the fluid viscosity and κ the permeability, and $q = \zeta\rho_f/\phi$, with ζ the tortuosity. It should be stressed that the thermo-strain coupling in Eq. (1) is only concerned with the bulk strain and is independent of the shear strain, this means the shear wave (S wave) is not affected by temperature changes (in homogeneous media). The equation

assumes that the solid and fluid phases have the same temperature.

To obtain the phase velocity and attenuation of the different wave modes, we consider the following plane-wave analysis by expressing the displacement and temperature as plane waves,

$$\begin{cases} u_i = As_i e^{\mathrm{i}\omega\left(t-\frac{l_j}{v_c}x_j\right)} \\ w_i = Bd_i e^{\mathrm{i}\omega\left(t-\frac{l_j}{v_c}x_j\right)} \\ T = Ce^{\mathrm{i}\omega\left(t-\frac{l_j}{v_c}x_j\right)} \end{cases}, \tag{2}$$

where A, B and C are amplitude constants, s_i and d_i are vectors, ω is the angular frequency, v_c is the complex velocity, t is the travel time, l_j denotes the propagation directions, x_j are the position components, and $\mathrm{i} = \sqrt{-1}$.

Substituting Eq. (2) into (1) and considering P-wave propagation parallel to the direction of displacement (i.e., $s_i l_i = d_i l_i = 1$), we obtain the dispersion relation (Wei et al., 2020),

$$b_1\left(v_c^2\right)^3 + b_2\left(v_c^2\right)^2 + b_3 v_c^2 + b_4 = 0, \tag{3}$$

where

$$\begin{cases} b_1 = \rho C_e \phi N(\omega L - \mathrm{i}r\rho) \\ b_2 = \mathrm{i}\phi rK - \omega(r\phi(\gamma\rho + \tau K) + \phi\rho cH + T_0\beta J) - \mathrm{i}\omega^2(\phi(\gamma L + \rho C_e H\tau) + T_0\beta J\tau) \\ b_3 = \omega(\phi(\rho C_e ME + r\gamma F) + T_0\beta G) + \mathrm{i}\omega^2(\phi(\gamma H + \rho C_e ME\tau) + T_0\beta G\tau) \\ b_4 = -\mathrm{i}\omega^2\gamma\phi ME \end{cases}, \tag{4}$$

with

$$\begin{cases} E = \lambda + 2\mu, F = E + \alpha^2 M, G = E\beta_f + M(\alpha - 1)(\alpha\beta_f - \phi\beta) \\ H = qF + \rho M - 2\alpha M\rho_f, J = \beta_f(\rho - \rho_f) + \phi\beta(q - \rho_f), K = \rho cF + T_0\beta^2 \\ L = q\rho - \rho_f^2, N = 1 + i\omega\tau \end{cases} \tag{5}$$

These equations analytically describe the dispersion and attenuation characteristics of wave propagation in thermo-poroelastic media. It should be emphasized that the fast-P wave is dissipative as the coupling with the fluid and heat flow. By setting $\beta = \beta_f = 0$, we obtain a quadratic equation for v_c, which corresponds to Biot velocities for the fast- and slow-P waves:

$$\left(-\mathrm{i}b_\rho + \omega m_\rho - \omega\rho_f^2\right)v_c^4 + \left(\mathrm{i}bE_G - \omega mE_G - \omega M_\rho + 2\omega\alpha M_{\rho f}\right)v_c^2 + \omega ME = 0, \tag{6}$$

and an additional root for the thermal wave,

$$v_c = \sqrt{\frac{\mathrm{i}\omega a^2}{1 + \mathrm{i}\omega\tau}} \text{ and } a = \sqrt{\frac{\gamma}{c}}, \tag{7}$$

where a is the thermal diffusivity (Carcione et al., 2019). The phase velocity and attenuation factor can be obtained from the complex velocity as

$$v_p = \left[\mathrm{Re}\left(v_c^{-1}\right)\right]^{-1} \text{ and } A = -\omega\mathrm{Im}\left(v_c^{-1}\right) \tag{8}$$

2.2. The AVO method

Fig. 1 shows a diagram of the reflection and transmission of an inhomogeneous plane wave incident at an interface between two thermo-poroelastic media. We use the superscripts I and II to denote the incidence ($z > 0$) and transmission ($z < 0$) media. The incident wave generates reflected fast P (RP1), Biot slow P (RP2), thermal slow P (RT), and shear (RS) waves in the upper-medium I and four transmitted waves in the lower-medium II. The eight boundary conditions between the two half-spaces ($z = 0$) are (Ignaczak and Ostoja-Starzewski, 2010)

$$\begin{cases} u_z^{\mathrm{I}} = u_z^{II},\ u_x^{\mathrm{I}} = u_x^{II},\ \sigma_{zz}^{\mathrm{I}} = \sigma_{zz}^{II},\ \sigma_{xz}^{\mathrm{I}} = \sigma_{xz}^{II} \\ \phi^{\mathrm{I}}\left(w_z^{\mathrm{I}} - u_z^{\mathrm{I}}\right) = Q\phi^{II}\left(w_z^{II} - u_z^{II}\right), Qp^{\mathrm{I}} = Qp^{II} + (1 - Q)\phi^{II}\left(w_z^{II} - u_z^{II}\right) \\ T^{\mathrm{I}} = T^{II}, \kappa^{\mathrm{I}}\frac{\partial T^{\mathrm{I}}}{\partial z} = \kappa^{II}\frac{\partial T^{II}}{\partial z} \end{cases}, \tag{9}$$

where $Q = 0$ and 1 denote impermeable (pores sealed) and permeable (pores open) boundaries, respectively.

The potential functions of plane waves for the case of P-wave incidence are

$$\begin{cases} \phi_s^l = \phi_0^s + \sum_{a=m}^{n}\phi_a^s,\ \phi_f^l = \phi_0^f + \sum_{a=m}^{n}\phi_a^f \\ \psi_s^l = \psi_b^s,\ \psi_f^l = \psi_b^f \end{cases}, \tag{10}$$

where for the incidence (reflection) medium (l denotes I), $m = 1$, $n = 3$, and $b = 4$, whereas for the transmission medium (l denotes II), $m = 5$, $n = 7$, $b = 8$, and the coefficients of the potential functions with subscript 0 are zero. The displacement potentials are

$$\begin{cases} \phi_a = A_a \exp[\mathrm{i}(\omega t - \mathbf{k}_a \bullet \mathbf{x})], a = 0, 1, \ldots, 7 \text{ and } \neq 4 \\ \psi_b = A_b \exp[\mathrm{i}(\omega t - \mathbf{k}_b \bullet \mathbf{x})], b = 4, 8 \end{cases} \tag{11}$$

The wave vectors are

$$\mathbf{k}_c \bullet \mathbf{x} = p_c x + q_c z, c = 0, 1, \ldots 8, \tag{12}$$

where the horizontal wavenumber p_c remains unchanged during the propagation, following the generalized Snell law (Borcherdt, 2009) with

$$p_c = |k|\sin\theta - \mathrm{i}|\alpha|\sin(\theta - \gamma) \tag{13}$$

The vertical wavenumber q_c can be obtained from the complex wavenumbers k_c as

$$q_c = D_R + \mathrm{i}D_I, D = \pm pv\sqrt{k_c^2 - p_c^2}, \tag{14}$$

where pv denotes the principal value. The downward waves correspond to the minus sign otherwise the positive sign holds to guarantee the decay of the reflected and transmitted waves down the positive z-direction.

Substituting the constitutive relation and the potential functions into the boundary conditions, the Knott equations for incident P wave is obtained as

$$\begin{bmatrix} a_{11} & a_{12} & a_{13} & a_{14} & a_{15} & a_{16} & a_{17} & a_{18} \\ a_{21} & a_{22} & a_{23} & a_{24} & a_{25} & a_{26} & a_{27} & a_{28} \\ a_{31} & a_{32} & a_{33} & a_{34} & a_{35} & a_{36} & a_{37} & a_{38} \\ a_{41} & a_{42} & a_{43} & a_{44} & a_{45} & a_{46} & a_{47} & a_{48} \\ a_{51} & a_{52} & a_{53} & a_{54} & a_{55} & a_{56} & a_{57} & a_{58} \\ a_{61} & a_{62} & a_{63} & a_{64} & a_{65} & a_{66} & a_{67} & a_{68} \\ a_{71} & a_{72} & a_{73} & a_{74} & a_{75} & a_{76} & a_{77} & a_{78} \\ a_{81} & a_{82} & a_{83} & a_{84} & a_{85} & a_{86} & a_{87} & a_{88} \end{bmatrix} \begin{bmatrix} A_1/A_0 \\ A_2/A_0 \\ A_3/A_0 \\ A_4/A_0 \\ A_5/A_0 \\ A_6/A_0 \\ A_7/A_0 \\ A_8/A_0 \end{bmatrix} = \begin{bmatrix} a_{19} \\ a_{29} \\ a_{39} \\ a_{49} \\ a_{59} \\ a_{69} \\ a_{79} \\ a_{89} \end{bmatrix}, \tag{15}$$

where

$$
\begin{cases}
a_{11}=q_1, a_{12}=q_2, a_{13}=q_3, a_{14}=p_4,\\
a_{15}=q_5, a_{16}=q_6, a_{17}=q_7, a_{18}=-p_8,\\
a_{19}=q_0, a_{21}=p_1, a_{22}=p_2, a_{23}=p_3, a_{24}=-q_4,\\
a_{25}=-p_5, a_{26}=-p_6, a_{27}=-p_7, a_{28}=-q_8, a_{29}=-p_0\\
a_{31}=k_1^2\Big(-M^{\mathrm{I}}(\alpha^{\mathrm{I}})^2-M^{\mathrm{I}}\alpha^{\mathrm{I}}V_1-\lambda^{\mathrm{I}}\Big)+\delta_1\beta^{\mathrm{I}}(\mathrm{i}\omega_{T1}-1)-2\mu^{\mathrm{I}}q_1^2,\\
a_{32}=k_2^2\Big(-M^{\mathrm{I}}(\alpha^{\mathrm{I}})^2-M^{\mathrm{I}}\alpha^{\mathrm{I}}V_2-\lambda^{\mathrm{I}}\Big)+\delta_2\beta^{\mathrm{I}}(\mathrm{i}\omega_{T1}-1)-2\mu^{\mathrm{I}}q_2^2,\\
a_{33}=k_3^2\Big(-M^{\mathrm{I}}(\alpha^{\mathrm{I}})^2-M^{\mathrm{I}}\alpha^{\mathrm{I}}V_3-\lambda^{\mathrm{I}}\Big)+\delta_3\beta^{\mathrm{I}}(\mathrm{i}\omega_{T1}-1)-2\mu^{\mathrm{I}}q_3^2,\\
a_{34}=-2\mu^{\mathrm{I}}p_4q_4,\\
a_{35}=k_5^2\Big(-M^{II}(\alpha^{II})^2-M^{II}\alpha^{II}V_5-\lambda^{II}\Big)+\delta_5\beta^{II}(\mathrm{i}\omega_{T1}-1)-2\mu^{II}q_5^2,\\
a_{36}=k_3^2\Big(-M^{II}(\alpha^{II})^2-M^{II}\alpha^{II}V_6-\lambda^{II}\Big)+\delta_6\beta^{II}(\mathrm{i}\omega_{T1}-1)-2\mu^{II}q_3^2,\\
a_{37}=k_3^2\Big(-M^{II}(\alpha^{II})^2-M^{II}\alpha^{II}V_7-\lambda^{II}\Big)+\delta_7\beta^{II}(\mathrm{i}\omega_{T1}-1)-2\mu^{II}q_3^2,\\
a_{38}=-2\mu^{II}p_8q_8,\\
a_{39}=k_0^2\Big(M^{\mathrm{I}}(\alpha^{\mathrm{I}})^2+M^{\mathrm{I}}\alpha^{\mathrm{I}}V_0+\lambda\Big)-\delta_0\beta^{\mathrm{I}}(\mathrm{i}\omega_{T1}-1)+2\mu^{\mathrm{I}}q_0^2,\\
a_{41}=2\mu^{\mathrm{I}}p_1q_1,\ a_{42}=2\mu^{\mathrm{I}}p_2q_2,\ a_{43}=2\mu^{\mathrm{I}}p_3q_3,\ a_{44}=\mu^{\mathrm{I}}\big(p_4^2-q_4^2\big),\\
a_{45}=2\mu^{II}p_5q_5,\ a_{46}=2\mu^{II}p_6q_6,\ a_{47}=2\mu^{II}p_7q_7,\\
a_{48}=-\mu^{II}\big(p_8^2-q_8^2\big),\ a_{49}=2\mu^{\mathrm{I}}p_0q_0,\\
a_{51}=\phi^{\mathrm{I}}q_1(V_1-1),\ a_{52}=\phi^{\mathrm{I}}q_2(V_2-1),\ a_{53}=\phi^{\mathrm{I}}q_3(V_3-1),\\
a_{54}=\phi^{II}p_4(V_4-1),\ a_{55}=\phi^{II}q_5(V_5-1),\ a_{56}=\phi^{II}q_5(V_5-1),\\
a_{57}=\phi^{II}q_7(V_7-1),\ a_{58}=-\phi^{II}p_8(V_8-1),\ a_{59}=\phi^{\mathrm{I}}q_0(V_0-1),\\
a_{61}=k_1^2M^{\mathrm{I}}(V_1+\alpha^{\mathrm{I}})-\dfrac{\delta_1\beta_f^{\mathrm{I}}}{\phi^{\mathrm{I}}}(\mathrm{i}\omega_{T2}-1),\\
a_{62}=k_2^2M^{\mathrm{I}}(V_2+\alpha^{\mathrm{I}})-\dfrac{\delta_2\beta_f^{\mathrm{I}}}{\phi^{\mathrm{I}}}(\mathrm{i}\omega_{T2}-1),\\
a_{63}=k_3^2M^{\mathrm{I}}(V_3+\alpha^{\mathrm{I}})-\dfrac{\delta_3\beta_f^{\mathrm{I}}}{\phi^{\mathrm{I}}}(\mathrm{i}\omega_{T2}-1),\\
a_{64}=0,\ a_{68}=0,\\
a_{65}=-k_5^2M^{II}(V_5+\alpha^{II})-\dfrac{\delta_5\beta_f^{II}}{\phi^{II}}(\mathrm{i}\omega_{T21}-1),\\
a_{66}=-k_6^2M^{II}(V_6+\alpha^{II})-\dfrac{\delta_6\beta_f^{II}}{\phi^{II}}(\mathrm{i}\omega_{T21}-1),\\
a_{67}=-k_7^2M^{II}(V_7+\alpha^{II})-\dfrac{\delta_7\beta_f^{II}}{\phi^{II}}(\mathrm{i}\omega_{T21}-1),\\
a_{69}=-k_0^2M^{\mathrm{I}}(V_0+\alpha^{\mathrm{I}}),\ a_{71}=\delta_1,\ a_{72}=\delta_2,\ a_{73}=\delta_3,\\
a_{74}=0,\ a_{75}=\delta_5,\ a_{76}=\delta_6,\ a_{77}=\delta_7,\ a_{78}=0,\\
a_{79}=-\delta_0,\ a_{81}=\gamma^{\mathrm{I}}\delta_1q_1,\ a_{82}=\gamma^{\mathrm{I}}\delta_2q_2,\ a_{83}=\gamma^{\mathrm{I}}\delta_3q_3,\ a_{84}=0,\\
a_{85}=\gamma^{II}\delta_5q_5,\ a_{86}=\gamma^{II}\delta_6q_6, a_{87}=\gamma^{II}\delta_7q_7,\ a_{88}=0,\\
a_{89}=\gamma^{\mathrm{I}}\delta_0q_0,
\end{cases}
\tag{16}
$$

and

$$
\begin{cases}
V_a=\dfrac{\beta\bar{\phi}\bar{\tau}_1\big(M\bar{\alpha}\big(p_0^2+q_0^2\big)-\omega^2\rho_f\big)-\bar{\tau}_2\beta_f\big((E+\bar{\alpha}^2M)\big(p_0^2+q_0^2\big)-\rho\omega^2\big)}{\beta\bar{\phi}\bar{\tau}_1\big(m\omega^2+\mathrm{i}b\omega-M\big(p_0^2+q_0^2\big)\big)+\bar{\tau}_2\beta_f\big(M\bar{\alpha}\big(p_0^2+q_0^2\big)-\omega^2\rho_f\big)}\\
\delta_a=\dfrac{\mathrm{i}\omega\beta\bar{\tau}_4T_0(1+V_a)\big(p_0^2+q_0^2\big)}{\mathrm{i}\omega\bar{\tau}_2c-\bar{\gamma}\big(p_0^2+q_0^2\big)},a=0,1,\ldots,7\text{ and }\neq4\\
V_b=\dfrac{-\omega\rho_f}{m\omega+\mathrm{i}\eta/\bar{\kappa}},b=4,8
\end{cases}
\tag{17}
$$

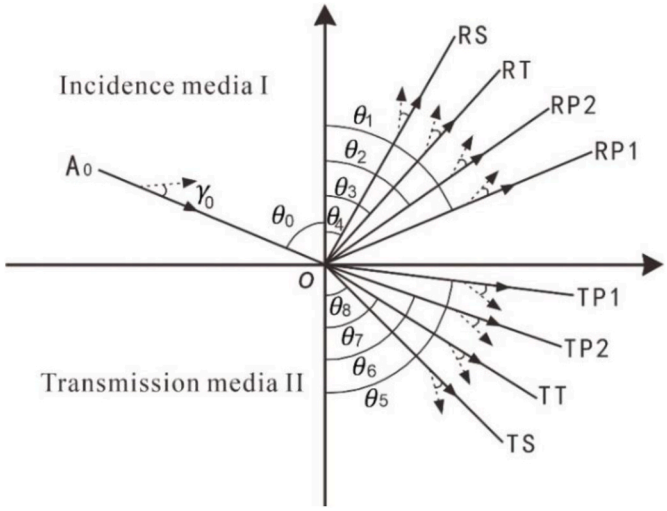

Fig. 1. Scheme of the reflection and transmission of inhomogeneous plane waves at an interface between two thermo-poroelastic media, where γ_0 is the incident-wave inhomogeneity angle between the attenuation (dashed arrow) and propagation (solid arrow) directions.

where $a=0, 1, 2, 3$ and $b=4$ correspond to the medium I (with superscript I), with $b=5$ to 8 to the medium II (with superscript II). After solving the linear system, we obtain the following R/T coefficients calculated by the complex wavenumber k_a (or k_b),

$$
\begin{cases}
R_a=\dfrac{A_a}{A_0}\dfrac{k_a}{k_0}=|R_a|\exp(\mathrm{i}\vartheta_a),a=1,2.3,4,\\
T_b=\dfrac{A_b}{A_0}\dfrac{k_b}{k_0}=|T_b|\exp(\mathrm{i}\vartheta_b),a=5,6,7,8,
\end{cases}
\tag{18}
$$

where $|R_a|$ and $|T_b|$ denote the R/T amplitudes and ϑ_a and ϑ_b are the corresponding phase angles. Eq. (18) formulates the R/T responses of an inhomogeneous plane wave incident at an interface between two thermo-poroelastic media.

3. Olkaria geothermal reservoirs

3.1. Geological setting

According to the drilling information and physico-chemical exploration, the Olkaria geothermal system is mainly associated with volcanic activities in the Late Quaternary (Omenda, 1998). Intense tectonic activity in the East African Rift Valley has resulted in the formation of several typical rift-volcanic geothermal systems distributed in the Kenyan Rift Valley (Fig. 2a). The Olkaria geothermal field, located in the southern end of the Kenyan, is considered to be one of the most promising with a total heating area of about 100 km^2 and a thermal storage depth of 500–3000 m. It has the highest heat storage temperature in Kenya, with an average temperature of 240 °C and a maximum recorded temperature of 380 °C (Zhang et al., 2018). According to the tectonic location, the Olkaria field can be divided into eastern, northeast, western, and dome regions (Fig. 2b). The deep rift activity led to a certain thinning of the crust and was compensated by the intrusion of magma from the Earth's mantle. Unsealed faults at the base of the rift valley formed a channel for subsequent volcanism, and much of the magma erupted along the faults, producing volcanic material that filled the rift valley. Overall, the Olkaria geothermal system is a volcanic complex traversed by positive faults, with deep graben fractures acting as upwelling channels for heat flow in the mantle and controlling the distribution of heat sources associated with shallow fractures (Karingithi et al., 2010).

3.2. Reservoir characteristics

Drilling reveals two sets of high-temperature reservoirs in the area (Mwaura and Kada, 2017). The first set is located 500 m underground with an average temperature of 180 °C, the second set is located 1500 m underground with a temperature above 300 °C. Fig. 3 shows the lithology and temperature profiles of the Olkaria West (Well 305), Olkaria East (Well 706 and 731 A), and Olkaria Domes (Well 916 and 918). Ground rock stratum is dominated by volcanic debris, basalt, and volcanic ash, which are products of past volcanic activities. The second layer is a regional cap of rhyolite and tuff with a wide distribution and low permeability. This is followed by the Olkaria thermal reservoir, which is separated by north-south trending fractures and dominated by Mau tuff in the western area and plateau trachyte in the eastern and dome-shaped area. Temperature logs show a large temperature gradient of up to 0.35 °C/m at depth, while temperatures at depth increase slowly with an average gradient of 0.075 °C/m. The reversal of the bottom temperature indicates a cold water injection. The temperature gradient in the eastern and dome-shaped part of the Olkaria field is slightly higher than that in the western part. Olkaria East is the next focus of geothermal development.

The lithology of volcanic formations is relatively stable, so the storage and transport of fluids are mainly controlled by petrophysical properties. Mau tuffs in the Olkaria West usually have high permeability with original pores and fractures, but are also sensitive to hydrothermal alteration that causes geothermal reservoirs being filled with secondary minerals. The resulting strong heterogeneity in porosity makes the production capacity of adjacent wells very different. The heat storage capacity in the eastern region depends on the degree of development of the tectonic fractures in the trachyte heat reservoir. In addition, the native cold shrinkage joints of trachyte reservoirs created by cooling-heating cycles due to hydrothermal extraction are also important channels for fluid storage and transport. Therefore, a better understanding of fluid and fracture distribution in thermal reservoirs is required to improve extraction efficiency and avoid short-circuiting of injected fluids. Thermo-poroelastic AVO analysis considering temperature effects is important for seismic monitoring of thermal reservoirs with different fracture densities and fluid contents.

It is worth mentioning that geophysical data, including gravity anomalies, magneto telluric and microseisms, have played a vital role in improving the conceptual model of the Olkaria geothermal field over the past decades (Axelsson et al., 2013; Rop, 2013). For example, microseismic data acquired from 1996 to 1998 provided valuable S-wave attenuation (Simiyu, 2000) to locate several large magma chambers at a depth of ~6 km beneath the Olkaria dome, northeast, and west production fields (see Fig. 2b). Intense microseismic activities are usually associated with high-temperature areas near the Quaternary volcanic centers, where the S-wave attenuation derived from microseismic data is sensitive to partially molten material (Carcione et al., 2020). Based on previous studies, we have updated the conceptual model of the western to eastern part of the Olkaria geothermal field, focusing on labeling the fluid channels (Fig. 4). The Olkaria geothermal system is a natural EGS where geothermal water is mainly derived from atmospheric precipitation along the main fractures and partly from infiltration. Cold water penetrates the bottom of the thermal reservoir, is transported laterally by temperature and pressure, heated and rises along the adjacent fractures. The temperature and pressure characteristics control the hydrothermal circulation, and the development of the fractures controls the hydrothermal direction. Fluids are mainly stored and transported in fracture zones and structural fractures in the form of a high-temperature thermal storage belt. Therefore, the density of the fractures is crucial for the capacity of the thermal reservoir. From a production perspective, north-south oriented wells have similar reservoir characteristics, while the productivity of east-west oriented wells can vary significantly even within a distance of only 300 m. Neighboring channels where hot water rises and channels where cold water falls can create large temperature differences even over short distances. Seismic AVO techniques are believed to be an effective tool for fracture prediction and fluid identification of thermal reservoirs if reflection data are available. To this purpose, we develop a thermo-poroelastic AVO method to simulate the AVO response of geothermal reservoirs. We further developed a practical petrophysical model based on previous researches of geothermal

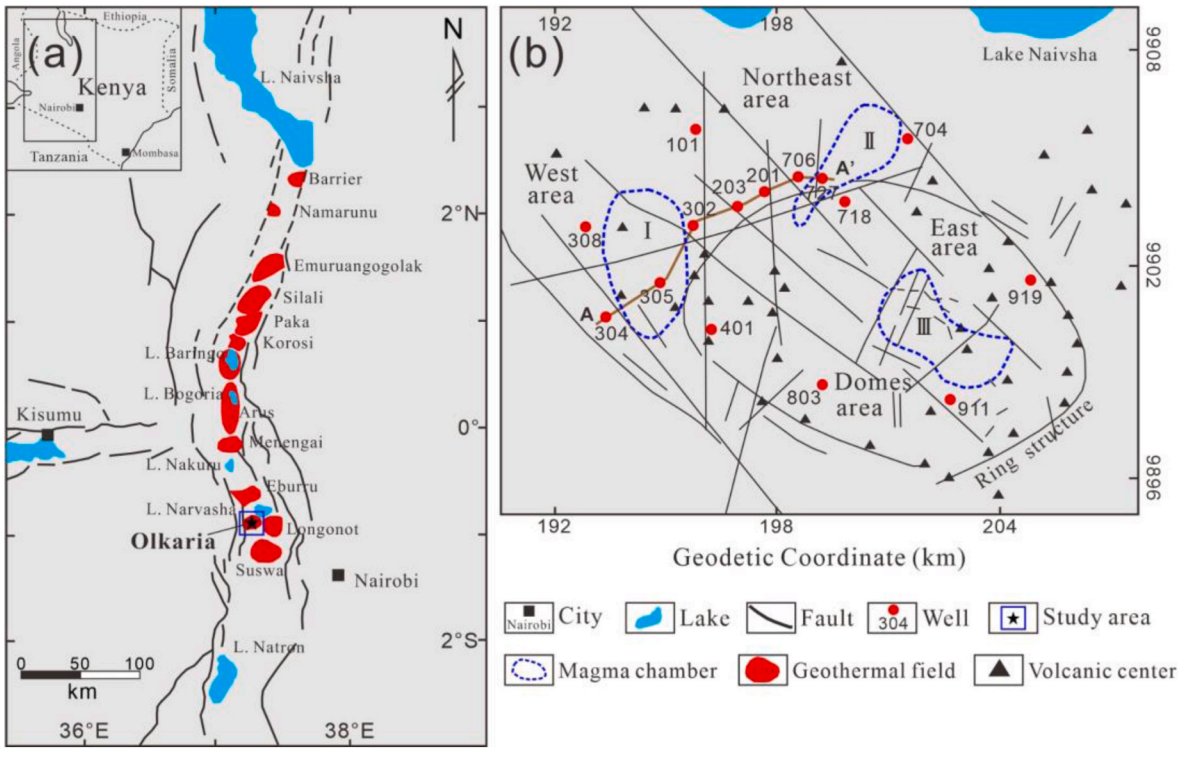

Fig. 2. Map of the geothermal belt in the Kenya Rift Valley (a) and the Olkaria geothermal field (b) (modified from Zhang et al., 2018).

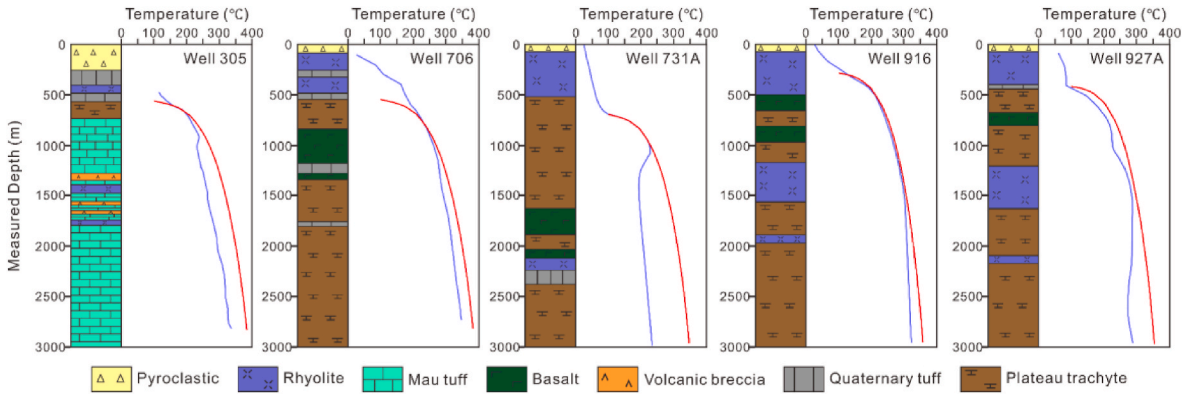

Fig. 3. Temperature and lithologic characteristics of the Olkaria West (Well 305), Olkaria East (Well 706 and 731 A), and Olkaria Domes (Well 916 and 918). The blue line is the formation temperature and the red line is the boiling curve. The original temperature data are from Rop (2013).

reservoirs in the Olkaria field.

4. Petrophysical model

The AVO approach is based on the R/T coefficients (see Fig. 1). An accurate model, with detailed lithological, petrophysical and thermophysical properties, and their spatial-time distributions, has not yet built for the Olkaria system. However, some preliminary models have been established by previous studies based on multidisciplinary and well-logging data. For instance, Axelsson et al. (2013) specify parameter ranges for a preliminary volumetric resource assessment of the system where the petrophysical properties are: rock porosity: 0.05–0.15, rock density (kg/m^3): 2500–3000, rock heat capacity (J/kg°C): 800–1000, water density (kg/m^3): 700–900, and water heat capacity (J/kg°C): 4800–6200. According to the porosity-permeability relationship of igneous rock, a porosity of 0.1 corresponds to an average permeability of 1 mD (Wang et al., 2015; Heap et al., 2018). In the Olkaria region, the permeability of the fracture zone can reach up to 200 darcy-meter, which is the main channel for hydrothermal upwelling. Igneous rocks in tectonically stabilized zones have lower permeability, varying with porosity from 0.1 mD-10 mD (Ofwona, 2002; Achini et al., 2022). Microseismic activities in this area are typically strong in high-temperature areas, especially near the Quaternary volcanic centers. Microseismic data collected by Simiyu (2000) were used to infer the average velocities of different-depth formations in the reservoirs: V_P = 2.8 km/s and V_S = 1.65 km/s at 0.6 km, 3.9 km/s and 2.28 km/s at 1.5 km, and 4.7 km/s and 2.66 km/s at 4 km.

To make the AVO analysis of the thermal reservoir more realistic, we create an accurate petrophysical model based on the actual conditions in the Olkaria area. That is, the thermal reservoir is dominated by trachyte (transmission medium) covered by basalt or rhyolite (impingement medium) at different depths (Fig. 3). First, we collected major element analysis data (using XRF) from representative Olkaria rocks (Macdonald et al., 2008; Marshall et al., 2009) and calculated the average values for each rock type (Table 1). The CIPW standard method of mineral calculation was used to determine the mineral composition of the rock (Whitman et al., 1902). In this classification, the percentages of oxides are converted into the number of oxide molecules, which are then combined according to the chemical analysis to form amounts of standard minerals (Lasheen et al., 2023). The mass fraction of each mineral can be determined by multiplying the number of atoms by the relative atomic mass, and the relative content is obtained by dividing the mass fraction by the mineral density (Table 2).

Trachyte consists mainly of feldspar minerals (84.41 %) with small amounts of quartz (10.76 %). Rhyolite has a comparable mineral composition, but with less feldspar (62.49%) and more quartz (31.98%) resulting from SiO_2 supersaturation. In addition to the high feldspar content (64.63%), the basalt is also characterized by high diopside (16.51%) and olivine minerals (12.53%). The effective grain bulk and shear moduli (K_s and μ_s) of the different rocks were determined from mineral content using the Voigt-Reuss-Hill (VRH) average. The dry-rock bulk modulus (K_m) and shear modulus (μ_m) are given by $K_m = (1-\phi)K_s/(1+c_m\phi)$ and $\mu_m = (1-\phi)\mu_s/(1+c_s\phi)$, where c_m and c_s are the bulk and shear consolidation coefficients (Ba et al., 2011).

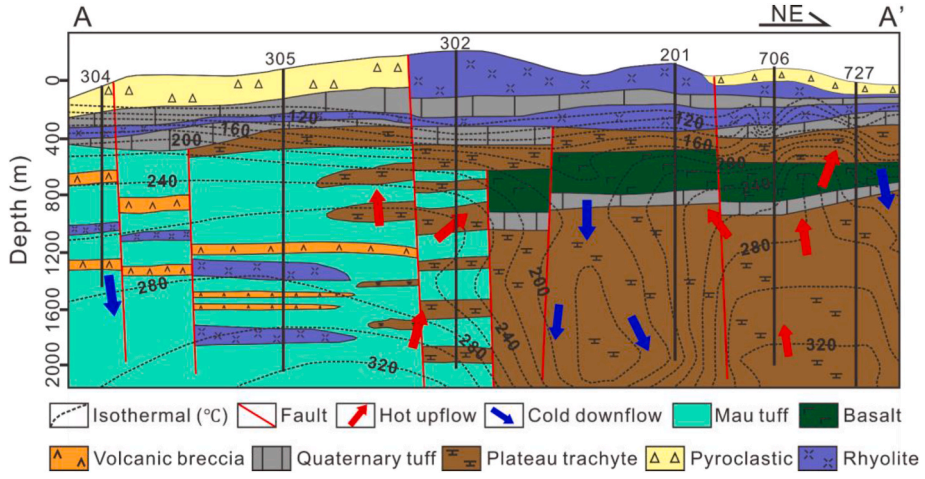

Fig. 4. Connected wells' lithology and temperature profile of the Olkaria geothermal field (A-A′ indicated by a blue line in Fig. 2b). The thermal storage lithologies are dominated by tuff in the western area and by trachyte in the eastern region. (modified from Shi et al., 2021).

In thermal reservoirs, the impact of thermal effects on rock properties cannot be neglected. Shallow thermal reservoirs at 180 °C, deep thermal reservoirs at 300 °C and a maximum reservoir temperature of 380 °C are the most concerned temperature conditions. And the elastic moduli of volcanic rocks decrease almost linearly with increasing temperature (below 500 °C) due to the decrease in rock strength and the formation of microcracks caused by thermal damage (Zhao et al., 2019), decreasing to 85% at 300 °C. The thermophysical properties of Olkaria thermal reservoir are described by Shi et al. (2021); Ofwona (2002).

The properties of the pore fluid are also important factors that affect the properties of the geothermal reservoir. In high-temperature environments, the transition from water to vapor phases depends on the pressure conditions in the formations. In the updraft channel of the heat flow (or in the geothermal well), there is a rapid pressure drop in the formation, which leads to the production of significant amounts of steam; naturally erupting steam can be observed in the Olkaria area. Formation boiling curves are commonly used to describe the critical temperature for the transition from water to steam phases under stratigraphic pressure conditions, where the high-temperature water begins to turn to steam at formation temperatures above the boiling curve. Fig. 3 shows the formation temperatures of several wells in the Olkaria area compared to boiling curves starting at 100 °C and showing a high temperature gradient. It can be seen that the formation temperatures in the shallow zone (<500 m) are close to the boiling curve and become increasingly lower than the boiling temperature with increasing depth. Even in the well with a high geothermal gradient (well 916), the formation temperatures at a depth of 2000 m do not reach the boiling temperature. Therefore, the pore fluid of the shallow reservoir with a high geothermal gradient is dominated by a mixture of steam and water, while the pore fluid of the deep reservoir with a low geothermal gradient contains high-temperature liquid water.

Based on the thermophysical properties of water (Lemmon et al., 2005), we consider a shallow reservoir (180 °C), with a pore-fluid density $\rho_{f1} = 500$ kg/m^3 and thermal conductivity $\gamma_{f1} = 0.36$ m kg/(s^3 °C); a deep reservoir (300 °C) with a liquid pore-fluid density $\rho_{f2} = 820$ kg/m^3 and thermal conductivity $\gamma_{f2} = 0.65$ m kg/(s^3 °C). In this way, we have obtained the petrophysical model of the thermal reservoir that corresponds to the actual context, all the parameters concerning the thermal reservoir are included in Table 3.

5. AVO response

In this section, we first analyze the dispersion and attenuation of waves in saturated trachyte thermal reservoir at 300 °C, based on the dispersion Eq (3) Frequency-dependent phase velocities and dissipation coefficients are calculated to illustrate the effect of thermophysical parameter and porosity on the fast P, Biot P, and thermal P waves. Thermal conductivity is considered the most essential property for characterizing the heat-transfer capability of the rock. It depends not only on the mineral composition, but also on their distribution, shape, internal structure, temperature etc. The thermal conductivity of the trachyte reservoir in different regions of Olkaria is 1.9–2.6 m kg/(s^3•°C) (Shi et al., 2021; Ofwona, 2002). To better reflect the effect of thermal conductivity variations, we consider granite thermal reservoirs with thermal conductivity values up to 3.2–4.6 m kg/(s^3•°C) (Li et al., 2023). Therefore, Fig. 5 compares the velocities and dissipation coefficients of the fast P, Biot P, and thermal P waves for the thermal conductivities: 1.9, 3.2, and 4.5 m kg/(s^3• °C). Two inflection points, corresponding to the Biot and thermal peaks in the attenuation plot, can be observed in the velocity profile of fast P-wave. (Fig. 5a and b). The Biot peak is caused by friction between the fluid and the grains (Biot, 1956) and hardly depends on the thermal conductivity. In general, there are no variations in the low-frequency range. The high-frequency thermal attenuation peak increases notably with thermal conductivity increases, corresponding in a rise of fast P-wave velocity. The Biot slow P-wave follows a similar behavior (Fig. 5c and d), while the thermal slow P-wave velocity increases slightly (Fig. 5e and f). The low velocity and high attenuation of the thermal wave make it difficult to detect under normal conditions.

Specific heat is the amount of heat absorbed or released per unit mass under temperature variations. At the same temperature, a reservoir with a high specific heat stores more heat energy. Fig. 6 compares the phase velocities and dissipation coefficients of the fast-P, Biot slow-P, and thermal slow-P waves for the specific heats: 820, 920, and 1020 kg/(m•s^2• °C). We see that the fast-P velocity is highly affected, increasing with decreasing specific heat, while the Biot and thermal peaks show slight changes. The specific heat of rocks is attributed to lattice vibrations and particle thermal motion. Particularly, these vibrations become dominant at high temperatures and therefore, affect the fast-P velocity. Based on porosity variations in the Olkaria thermal reservoir (Axelsson et al., 2013), Fig. 7 compares the phase velocities and dissipation coefficients of the fast P, Biot slow P, and thermal slow P waves for the porosities: 0.05, 0.10, and 0.15. As anticipated, the fast-P wave velocity

Table 1
Major element analyses of representative Olkaria rocks.

Rock types	Trachyte	Basalt	Rhyolite
SiO_2	65.07	49.08	74.89
TiO_2	0.51	1.61	0.15
Al_2O_3	16.33	15.96	11.42
FeO	4.96	10.50	2.82
MnO	0.15	0.17	0.06
MgO	0.23	7.20	0.05
CaO	1.50	10.86	0.29
Na_2O	5.17	2.82	5.21
K_2O	5.62	1.18	4.65
P_2O_5	0.06	0.34	0.01
Sum	99.60	99.72	99.55

Table 2
Standard mineral composition of representative Olkaria rocks. Or Orthoclase, Ab Albite, An Anorthite, Qz Quartz, Ap Apatite, Il Ilmenite, Mt Magnetite, Hy Hyperthene, Di Diopside, Wo Wollastonite, Ol Olivine, Ac Acmite.

Rock types	Trachyte	Basalt	Rhyolite
Or	35.016	8.131	28.823
Ab	44.771	26.978	33.668
An	4.619	29.523	–
Qz	10.765	–	31.984
Ap	0.123	0.736	0.019
Il	0.771	2.674	0.161
Mt	2.684	1.695	0.669
Hy	–	1.227	–
Di	0.965	16.510	0.212
Wo	0.285	–	0.405
Ol	–	12.525	–
Ac	–	–	4.058

Table 3
Thermal reservoir petrophysical model. κ permeability, ι tortuosity, C_e bulk specific heat, β thermoelasticity coefficient, γ thermal conductivity, τ relaxation time.

Property	Trachyte	Basalt	Rhyolite
K_s GPa	42	58	40
μ_s GPa	20	28	24
ρ_s kg/m^3	2750	2850	2650
ϕ	0.10	0.10	0.10
K_m GPa	19	26	18
μ_m GPa	9	13	11
κ mD	1	1	1
ι	2	2	2
C_e (m s^2 °C)	1020	820	820
β kg/(m s^2 °C)	$2.4 \bullet 10^6$	$1.2 \bullet 10^6$	$1.2 \bullet 10^6$
γ m kg/(s^3 °C)	2.5	2	2
τ s	1.5×10^{-8}	1.5×10^{-8}	1.5×10^{-8}

significantly diminishes with increasing porosity. The Biot attenuation moves to higher frequencies, whereas the thermal attenuation increases with increasing porosity. Dispersion occurs at frequencies (10^2~10^4 Hz) and higher than 10^8 Hz for the Biot P and thermal P waves, respectively.

We conduct the AVO modeling based on Eq (18) where the R/T coefficients of the fast-P wave (RP1, TP1), slow-P wave (RP2, TP2), T wave (RPT, TPT), and S wave (RPS, TPS) are formulated for an interface between two thermo-poroelastic media. The angle-dependent R/T responses for two cover layers (basalt and rhyolite) was calculated at different temperature conditions in the case of an incident P-wave. Three temperature conditions, 180 °C, 300 °C and 380 °C, were chosen to represent the shallow steam-water mixing zone (500 m), the deep high-temperature fluid zone (1500 m) and the maximum reservoir temperature zone (2500 m) of the Olkaria geothermal system, respectively. The petrophysical modeling properties of the fluids and rocks change with the different formation conditions.

Fig. 8 shows the R/T coefficients with rhyolite cover. The modulus and density of the trachyte reservoir are slightly higher than those of the rhyolite cover, leading to the presence of a critical angle in the R/T responses. The critical angle is around 60° in the shallow zone with lower temperatures and increases slightly with increasing temperature. Fig. 9 shows the R/T coefficients with basalt coverage, where there is no critical angle for a large impedance on a medium with small impedance. The fast P-wave reflection coefficient (RP1) is relatively low due to the small impedance difference between the capping layer and the geothermal reservoir, while the slow P-wave R/T coefficients (RP2, TP2) are mainly influenced by the fluid properties. Shallow pore fluids are low modulus and low density vapor-water mixtures, while deeper formations have higher pressures and the pore fluids are maintained in the liquid phase at high temperature, resulting in a significantly higher RP2 in the deeper layers than in the shallower ones. Similarly, an increase in temperature and changes in fluid properties increase the R/T coefficients of the T-wave. It can be shown that the angle-dependent R/T coefficients are consistent with the conservation of energy. These AVO can be the foundation for the seismic interpretation of reflection amplitudes from thermo-poroelastic media.

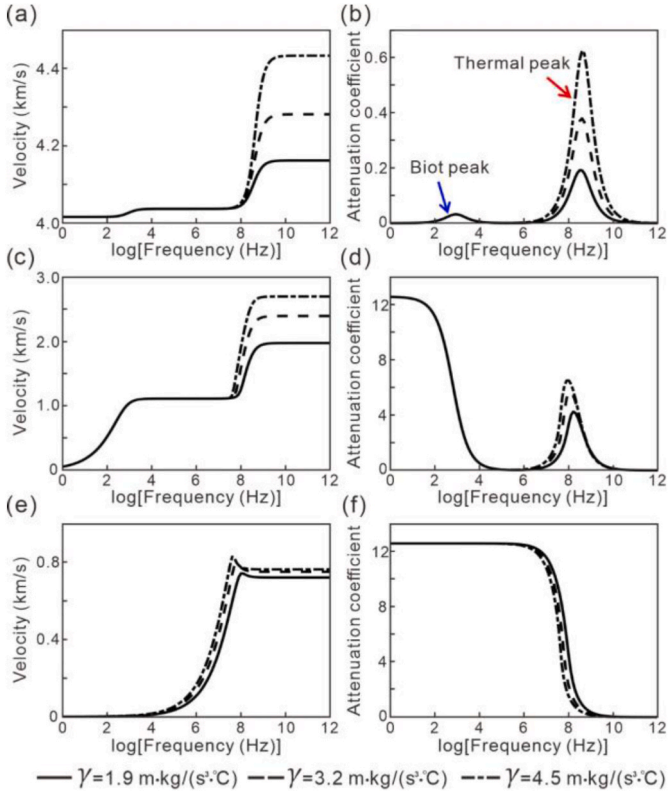

Fig. 5. Phase velocities (a, c, and e) and dissipation coefficients (b, d, f) as a function of frequency for the fast P (a, b), Biot slow P (c, d), and thermal slow P (e, f) waves of trachyte thermal reservoir at different thermal conductivities. The properties are listed in Table 3.

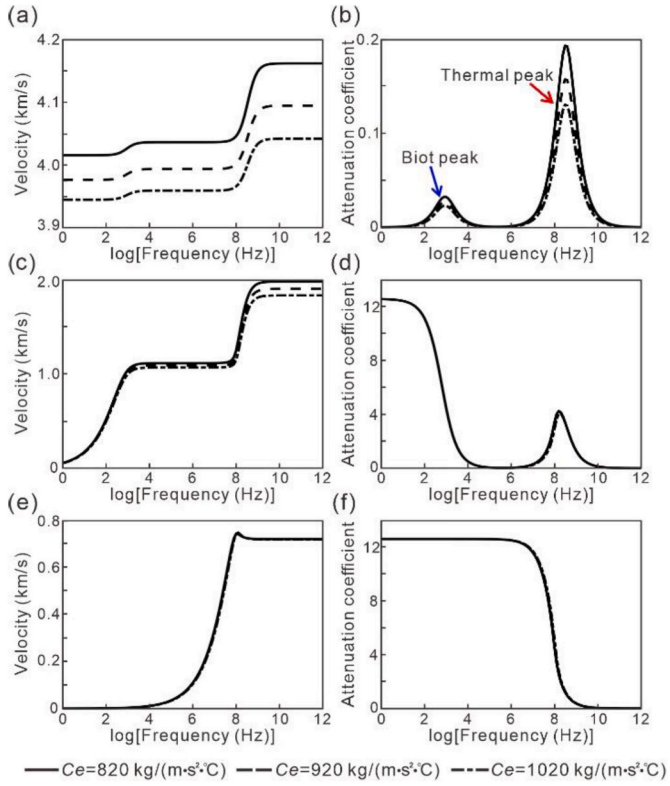

Fig. 6. Phase velocities (a, c, and e) and dissipation coefficients (b, d, f) as a function of frequency for the fast P (a, b), Biot slow P (c, d), and thermal slow P (e, f) waves of trachyte thermal reservoir at different specific heats. The properties are listed in Table 3.

Trachyte thermal reservoirs are less susceptible to hydrothermal erosion, and the evolution of porosity is mainly controlled by tectonic stress, which considerably influences heat flow distribution. Therefore, analyzing the R/T responses of thermal reservoirs with varying porosities helps in the precise further development of EGS. Fig. 10 shows the condition of the deep layer with liquid water (300 °C) and rhyolite cover, where the upper/lower medium porosity takes the values 0.1/0.05, 0.1/0.1, and 0.1/0.15, with the other properties keep constant. We see that increasing of ϕ^{II} reduces the modulus difference between caprock and reservoir, thus reducing the intercept and gradient of R_{P1} and R_{P2}, and enhancing the transmission energy of fast P-wave, and the critical angle has increased from 50° to 65°. The R_{PS} is essentially constant at small incidence angles and decreases significantly near the critical angle. In AVO inversion of seismic data, the fast-P reflection coefficient (R_{P1}) is the most useful. The above analysis highlights the impact of temperature on both the physical properties of the rock and pore fluids, which can ultimately affect R_{P1}. Changes in porosity also have a significant impact on the reflected P-wave. Clarifying the AVO response characteristics under different conditions is crucial to achieve accurate temperature and porosity inversion of geothermal reservoirs, which is of significant importance for geothermal development.

Supercritical CO_2 ($SCCO_2$) can replace water as a heat transfer fluid for EGS (Cao et al., 2016). $SCCO_2$ has a liquid density and a gaseous viscosity, with a diffusion coefficient much higher than that of water. In some cases, failed fracturing may result in the fluid not following the expected path into the thermal reservoir, leaving the pore space with air. Therefore, we compare the AVO responses of thermal reservoirs saturated by water, $SCCO_2$ and air (dry case). We consider: water: $\rho_f = 820$

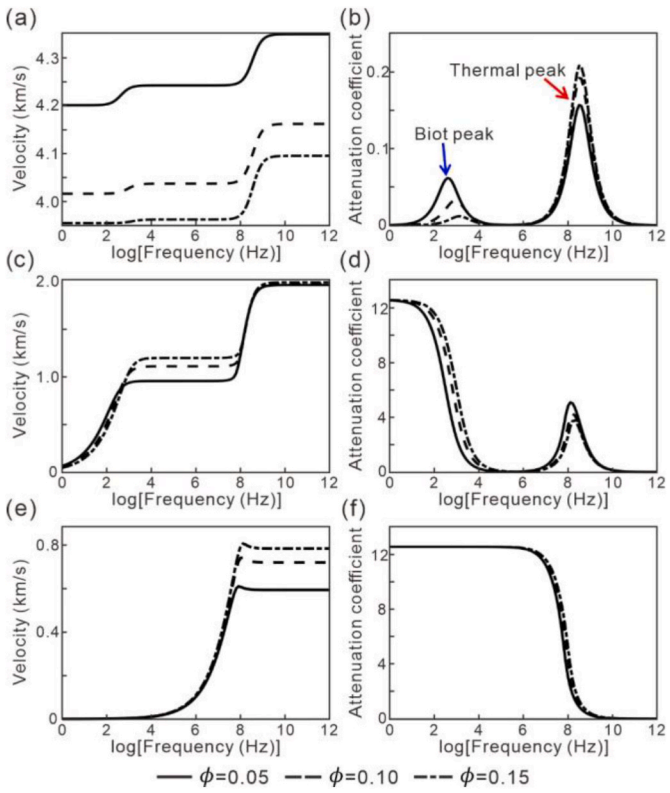

Fig. 7. Phase velocities (a, c, and e) and dissipation coefficients (b, d, f) as a function of frequency for the fast P (a, b), Biot slow P (c, d), and thermal slow P (e, f) waves of trachyte thermal reservoir at different porosities. The properties are listed in Table 3.

kg/m^3, $\eta_f = 0.001$ Pa s, and $\beta_f = 40000$ kg/(m s^2 °C); air: $\rho_f = 1.21$ kg/m^3, $\eta_f = 1.79*10^{-7}$ Pa s, and $\beta_f = 60000$ kg/(m s^2 °C); and $SCCO_2$: $\rho_f = 700$ kg/m^3, $\eta_f = 4*10^{-5}$ Pa s, and $\beta_f = 50000$ kg/(m s^2 °C). Fig. 11 shows the coefficients of the deep reservoir (300 °C) saturated by water, $SCCO_2$, and air, where we can see quite different behaviors depending on the type of fluid. For instance, supercritical CO_2 induces a larger critical angle than that of water, and the reservoir without fluid entry (air-saturated) has a higher reflection coefficient, gradient, intercept, and critical angle. These variations can be used to determine whether the heat recovery fluid is entering the correct channel within the EGS. Based on the changes in the R/T coefficients, seismic monitoring of EGSs could analyze fluid paths (water or dry) of fractures and further evaluate the quality of hydrofracturing, which is important for EGSs because many of them fail due to fluid leakage or short circuits.

Based on the analysis of the reflection and transmission coefficients, we have calculated the exact AVO result of the Olkaria geothermal reservoir. The thermo-poroelastic AVO was developed from the theory of elastic and thermoelastic AVO. The thermo-elastic AVO, which takes thermal effects into account, has been shown to be more accurate than the conventional elastic AVO under high temperature conditions (Hou et al., 2023). Fig. 12 compares synthetic common-shot gathers and the respective travel times between the three AVO methods described above, using the basalt cover of the geothermal field at 300 °C. The synthetic seismogram is obtained by convolution the respective exact equation and a Ricker wavelet with the main frequency 75 Hz in the time-angle domain, and the distance between the interface of thermo-poroelastic medium and the receivers is 100 m. We see that the thermo-poroelastic effect significantly changes both the travel time and amplitude of seismic responses. Compared to thermoelastic AVO modeling, thermo-poroelastic AVO modeling takes into account the porosity and the associated fluids as well as the thermal reaction of the pore fluid. The reduction of the integrated modulus and the impedance difference of the thermal reservoir and the cover layer increases the transit time of the AVO response and reduces the amplitude, especially at larger angles of incidence. These angle-dependent variations in amplitude and travel time of reflection events help provide information about the petrophysical properties. In general, the thermo-poroelastic AVO modeling considers the influence of thermal effect on wave propagation in porous rocks, which facilitates the prediction of petrophysical properties for thermal reservoirs.

6. Discussion

Enhanced geothermal system (EGS) through the artificial or natural circulation of fluids (e.g., water or CO2) involves a complex thermo-hydro-mechanical coupling (Rathnaweera et al., 2020). The cyclic recovery process often has the risk of fluid leakage and short circuits, and thus needs an assistance monitoring analysis for the distribution of hydrofracturing networks and fluid identification (Guo and Thurber, 2022). Seismic AVO, as a routine and efficient technique for the

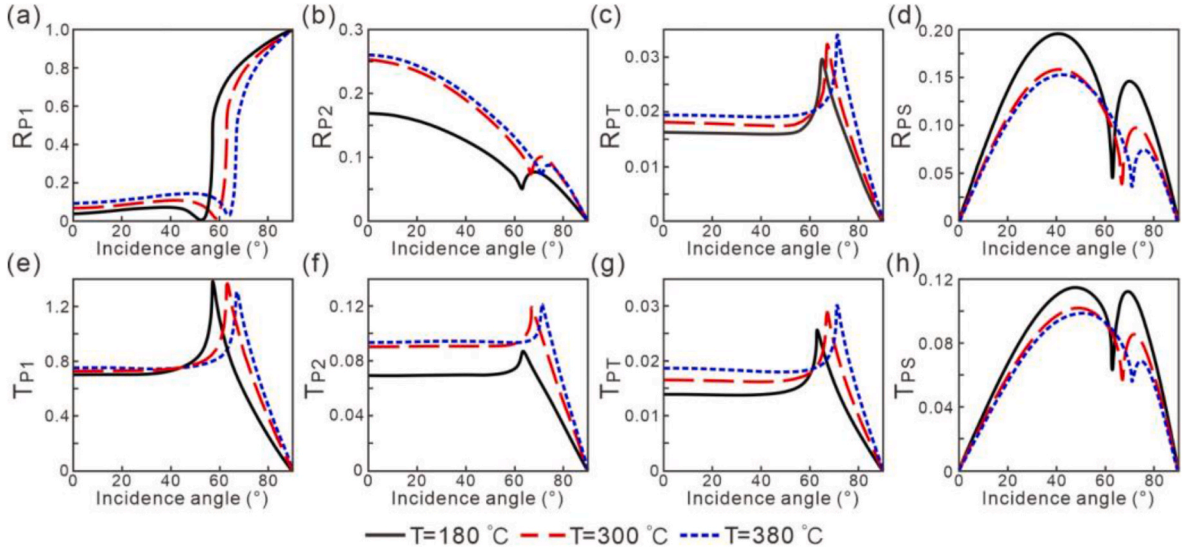

Fig. 8. Reflection (a, b, c, d) and transmission (e, f, g, h) amplitudes as a function of the P-wave incidence angle at different conditions with media temperatures of 180 °C, 300 °C, and 380 °C with rhyolite cover. The properties are listed in Table 3.

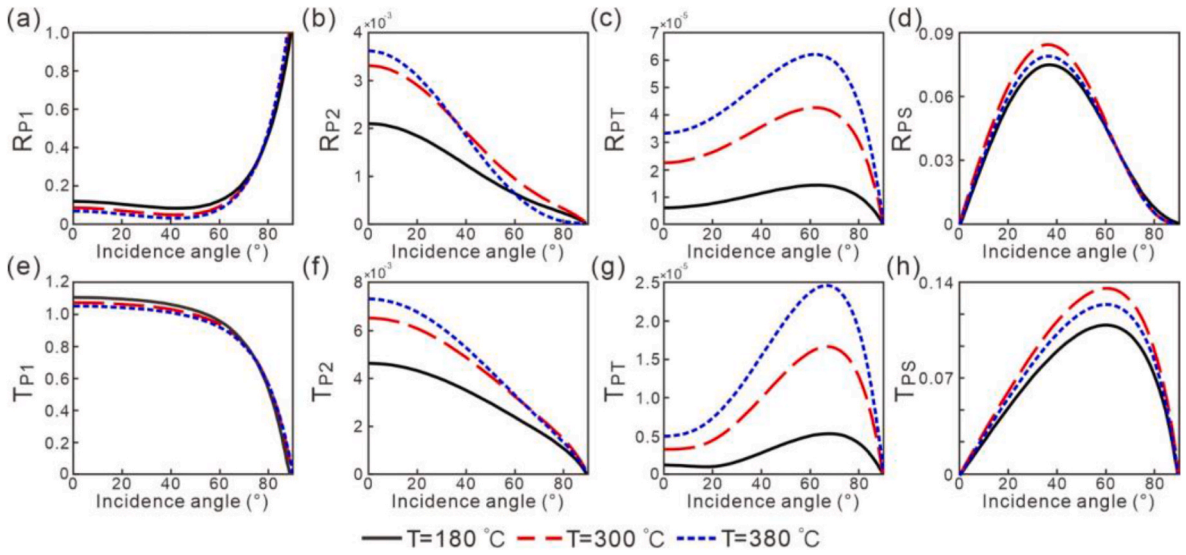

Fig. 9. Reflection (a, b, c, d) and transmission (e, f, g, h) amplitudes as a function of the P-wave incidence angle at different conditions with media temperatures of 180 °C, 300 °C, and 380 °C with basalt cover. The properties are listed in Table 3.

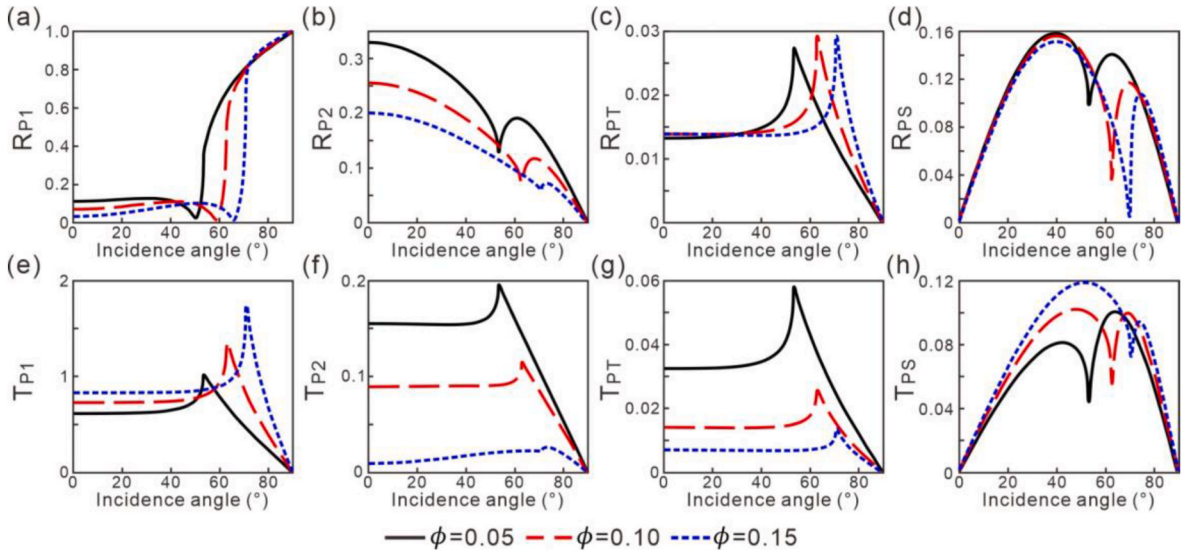

Fig. 10. Reflection (a, b, c, d) and transmission (e, f, g, h) amplitudes as a function of the P-wave incidence angle for the deep layer with liquid water (300 °C) and rhyolite cover, where the porosity varies as 0.05, 0.1, and 0.15. The properties are listed in Table 3.

exploration and development of conventional oil/gas resources (Fawad et al., 2020), has a significant potential for time-lapse monitoring the fluid distribution across hydrofracturing networks in EGSs. Conventional AVO techniques cannot be directly applied to thermal reservoirs because of neglecting the thermal effect on geophysical properties. We develop a thermo-poroelastic method for this task and conduct the AVO modeling of Olkaria geothermal reservoirs to investigate the effects of petrophysical and thermophysical properties of the natural EGS on the seismic reflection and transmission signature.

To our knowledge to date, as indicated in the chapter of Introduction, this is the only comprehensive AVO analyses of geothermal reservoirs. Unlike conventional oil/gas reservoirs, the properties of geothermal reservoirs and pore fluids vary with temperature and pressure conditions (Liu et al., 2018). According to the boiling curve of the Olkaria geothermal field, we divide the pore fluid into shallow mixture of steam and water and deep high-temperature liquid water, giving them different fluid parameters. Considering that the increase of temperature decreases rock strength and induces microcracks due to thermal damage (Zhao et al., 2019), we reduce the elastic moduli of trachyte thermal reservoirs approximately linearly with temperature (less than 500 °C). A plane-wave analysis with shows the effects of thermal conductivity, specific heat, and porosity on the velocity dispersion and attenuation of fast-P, Biot slow-P, and thermal slow-P waves. For temperatures less than 500 °C, limited changes in such thermophysical properties have negligible effects on wave propagation at seismic frequencies, whereas porosity has a pronounced effect as expected.

Then, we implement the thermo-poroelastic AVO modeling by P-wave incidence to investigate the effects of different thermal reservoir conditions on the R/T coefficients of induced fast-P, Biot slow-P, thermal slow-P, and S waves. We demonstrate that significant effects on the seismic reflection signature are from temperature, porosity, and fluid type. These variables help us to get more accurate information on thermal reservoir temperature and porosity. Among these petrophysical properties, the fluid type has the most pronounced effect, where water, SCCO2, and air (dry case) used as the heat transfer fluid, respectively, show distinct characteristics, enabling the AVO technique to be efficient

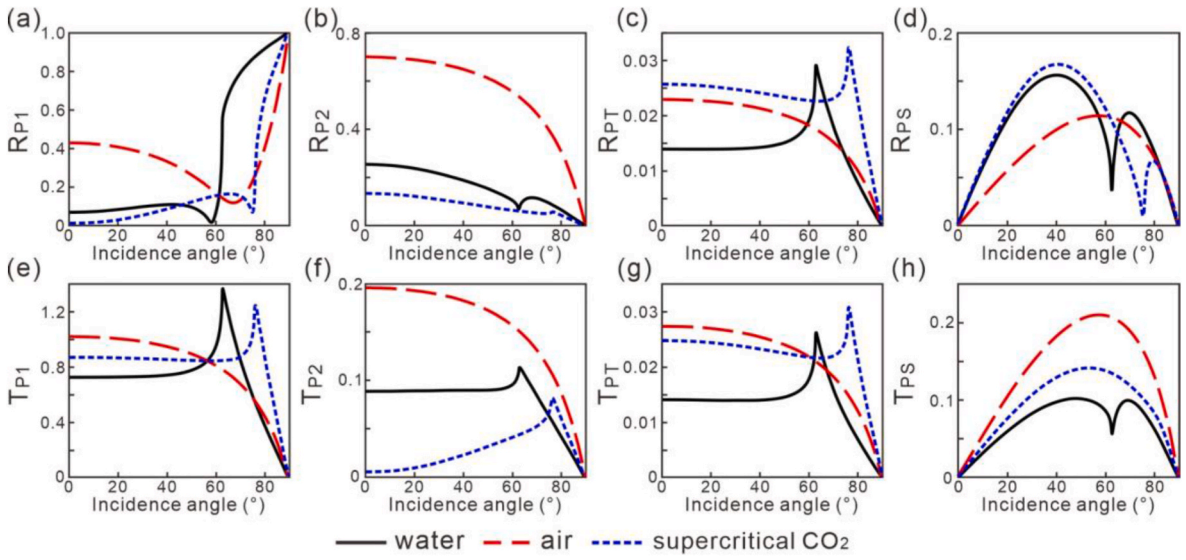

Fig. 11. Reflection (a, b, c, d) and transmission (e, f, g, h) amplitudes as a function of the P-wave incidence angle for the deep layer with liquid water (300 °C) and rhyolite cover, where the pore fluid varies as water, air and supercritical CO_2.

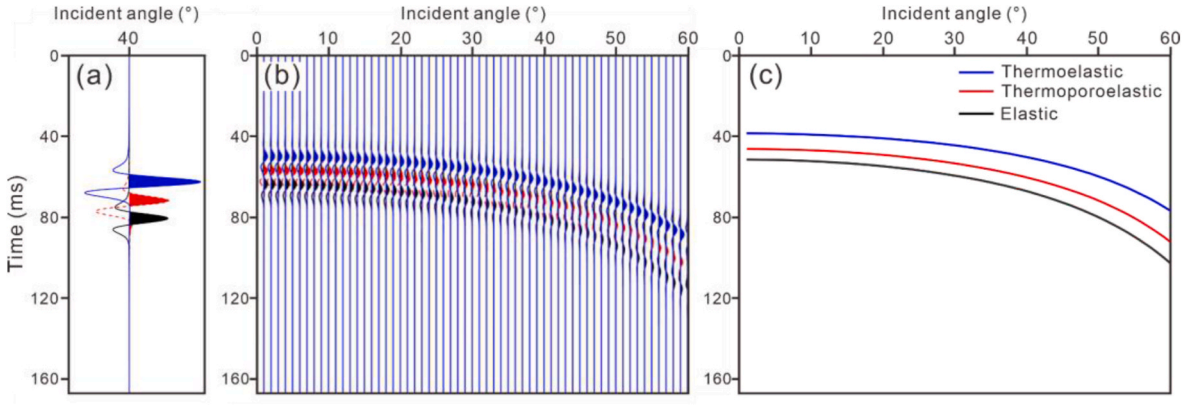

Fig. 12. Comparison of single seismic trace at 40° incidence angle (a), synthetic common-shot seismograms (b) of 75 Hz and the respective traveltimes (c), calculated by thermo-poroelastic, thermoelastic and conventional elastic AVO methods.

for fluid detection, which can be used as a precursor to hydrofracturing-induced permeability, fluid leakage or short circuits. Finally, we compare the AVO models of the elastic, thermoelastic and thermo-poroelastic theories. Thermo-poroelastic AVO more accurately represents the thermal reservoir information as it accounts for the combined impacts of thermal effects on the rock skeleton and pore fluids.

We should stress that practical geothermal reservoirs are more complex than our conceptual models aforementioned (Breede et al., 2013; Lu, 2018). In this sense, we actually conduct a conceptual AVO modeling of geothermal reservoirs. Specific potential assumptions for the calculation of R/T coefficients fall into the following several aspects. (1) The thermophysical properties of rocks, such as thermal conductivity, specific heat, and thermal expansivity, will not change with temperatures and pressures, which could be accepted for the temperature variations (less than 500 °C) of the Olkaria geothermal field. (2) The thermo-poroelastic AVO modeling incorporates the almost linear decrease of the thermal reservoir modulus due to thermal damage, without considering the elastic nonlinearity due to thermal expansion mismatch in multi-mineral rocks and thermally induced deformation of microcracks (Yang et al., 2021), which often occurs in volcanic rocks gradually with increasing temperature over 200 °C. The numerical differences are small enough not to influence the results significantly. (3) We consider simplified models of the physical properties of pore fluids under different temperature and pressure conditions. Variations of heat flow due to differences in the mineral content in different regions and the thermal alteration on the formation are complex requiring more data support and careful analysis. (4) The proposed AVO method is based on the theory of single-porosity thermo-poroelasticity, whereas typical thermal reservoirs are usually characteristic of stiff pores, fractures, and cracks (Vidal et al., 2017; Li et al., 2023). The resulting complex fractured-vuggy networks have quite different permeability, fluid leakage, and short circuits from those described by single-porosity thermo-poroelasticity in this paper. Incorporating the morphology of cracks and pores into AVO modeling is the next step in our program, and more petrophysical data from high-temperature/pressure rock physics and seismic monitoring data from geothermal fields are required to complete this work.

7. Conclusion

This research develops an AVO method based on the reflection and transmission (R/T) of elastic waves at an interface between two fluid-saturated thermo-poroelastic media. Conceptual petrophysical model was developed based on the lithological and temperature characteristics of the Olkaria geothermal field, and the fluid properties under different temperature conditions have been considered. The thermo-poroelastic

AVO modeling reveals the variation of R/T coefficients of geothermal reservoirs under different conditions. The main conclusions are obtained as follows:

(1) Plane wave analysis shows that limited changes in thermophysical properties have a negligible effect on wave propagation at seismic frequencies, whereas porosity has a pronounced effect as expected.
(2) Thermal reservoir temperature, porosity, and fluid type significantly affect seismic reflection signature, suggesting that the thermo-poroelastic AVO modeling can lead to more accurate thermal reservoir information and effective fluid monitoring.
(3) Synthetic seismic records produced from the thermo-poroelastic AVO method, taking into account pore and fluid thermal effects, prove to be more effective in predicting thermal reservoir petrophysical properties as compared to thermoelastic theory.

CRediT authorship contribution statement

Yifan Cheng: Writing – original draft, Visualization, Project administration, Methodology, Data curation. **Li-Yun Fu:** Writing – review & editing, Resources, Project administration, Methodology, Funding acquisition, Conceptualization. **Wanting Hou:** Validation, Software, Methodology, Data curation, Conceptualization. **José M. Carcione:** Writing – review & editing, Validation, Methodology, Formal analysis, Conceptualization. **Wubing Deng:** Writing – review & editing, Software, Resources, Project administration, Formal analysis. **Zhiwei Wang:** Writing – review & editing, Methodology, Data curation, Conceptualization.

Declaration of competing interest

The authors declare that they have no known competing financial interests or personal relationships that could have appeared to influence the work reported in this paper.

Data availability

Data will be made available on request.

Acknowledgements

The research is supported by the National Natural Science Foundation of China (Grant Nos. 42230803, 41821002) and 111 project "Deep-Superdeep Oil & Gas Geophysical Exploration" (B18055).

Appendix A

Lord and Shulman (1967) generalize Biot (1956) by introducing a relaxation time τ to the classical heat-conduction equation, which can be further extended for porous media as (Carcione et al., 2019; Wei et al., 2020)

$$\gamma T_{,ii} = \rho c\left(\dot{T} + \tau\ddot{T}\right) + \beta T_0\left[\left(\dot{u}_{i,i} + \dot{w}_{i,i}\right) + \tau\left(\ddot{u}_{i,i} + \ddot{w}_{i,i}\right)\right], \tag{A.1}$$

where T is the increment of temperature over a reference T_0, γ is the thermal conductivity, c is the specific heat, $\rho = (1-\phi)\rho_s + \phi\rho_f$ is the composite density with ρ_s and ρ_f the grain and fluid densities, ϕ is the bulk porosity. The displacement components u_i and w_i represent the solid and fluid phases, respectively. Thermal modulus $\beta = \beta_s + \alpha\beta_f$, with β_s and β_f represent the thermal stress coefficients of the solid and fluid phases. The dot above the variables indicates the time differentiation.

The constitutive relations of thermo-poroelasticity for the stress components σ_{ij}, displacement components (u_i and w_i), and pore-fluid pressure p_f are (Carcione et al., 2019)

$$\begin{cases} \sigma_{ij} = \lambda\delta_{ij}u_{k,k} + \mu\left(u_{i,j} + u_{j,i}\right) + \alpha M\delta_{ij}\left(\alpha u_{k,k} + w_{k,k}\right) - \beta\delta_{ij}T \\ -p_f = M\left(\alpha u_{i,i} + \omega_{i,i}\right) - \dfrac{\beta_f}{\phi}T \end{cases}, \tag{A.2}$$

where λ and μ are the Lamé constants of the drained matrix, δ_{ij} is the Kronecker delta, and

$$\begin{cases} \alpha = 1 - \dfrac{K_m}{K_s} \\ M = \dfrac{K_s}{1 - \phi - K_m/K_s + \phi K_s/K_f}, \\ K_m = \lambda + \dfrac{2}{3}\mu \end{cases} \tag{A.3}$$

where K_s and K_f are the solid and fluid bulk moduli.

References

AbuAisha, M., Loret, B., Eaton, D., 2016. Enhanced geothermal systems (EGS): hydraulic fracturing in a thermo-poroelastic framework. J. Pet. Sci. Eng. 146, 1179–1191. https://doi.org/10.1016/j.petrol.2016.07.027.

Achini, H.N., Adeigbe, O.C., Rop, B.K., 2022. Characterizing permeability from geological and geochemical data in the olkaria domes field in Kenya. East African Journal of Environment and Natural Resources 5 (1), 75–96. https://doi.org/10.37284/eajenr.5.1.594.

Anastasia, W.W., 2014. Geophysical survey of a high-temperature field, Olkaria. In: Presented at Short Course IX on Exploration for Geothermal Resources. Nov, pp. 2–24.

Angus, D.A., Dutko, M., Kristiansen, T.G., et al., 2015. Integrated hydro-mechanical and seismic modelling of the Valhall reservoir: a case study of predicting subsidence, AVOA and microseismicity. Geomech Energy Envir 2, 32–44. https://doi.org/10.1016/j.gete.2015.05.002.

Axelsson, G., Arnaldsson, A., Armannsson, H., et al., 2013. Updated conceptual model and capacity estimates for the greater olkaria geothermal system, Kenya. In:

Proceedings of the 38th Workshop on Geothermal Reservoir Engineering. SGP-TR-198, pp. 1–16.
Ba, J., Carcione, J.M., Nie, J.X., 2011. Biot-Rayleigh theory of wave propagation in double-porosity media. JGR: Solid Earth 116, B06202. https://doi.org/10.1029/2010JB008185.
Baldonedo, J., Bazarra, N., Fernández, J.R., Quintanilla, R., 2020. An a priori error analysis of a Lord-Shulman poro-thermoelastic problem with micro temperatures. Acta Mech. 231, 4055–4076. https://doi.org/10.1007/s00707-020-02738-z.
Batzle, M.L., Wang, Z., 1992. Seismic properties of pore fluids. Geophysics 57 (11), 1396–1408. https://doi.org/10.1190/1.1443207.
Biot, M.A., 1956. Thermoelasticity and irreversible thermodynamics. J. Appl. Phys. 27, 240–253.
Borcherdt, R.D., 2009. Viscoelastic Waves in Layered Media. Cambridge University Press.
Breede, K., Dzebisashvili, K., Liu, X., Falcone, G., 2013. A systematic review of enhanced (or engineered) geothermal systems: past, present and future. Geoth. Energy 1 (1), 1–27. https://doi.org/10.1186/2195-9706-1-4.
Cao, W.J., Huang, W.B., Jiang, F.M., 2016. Numerical study on variable thermophysical properties of heat transfer fluid affecting EGS heat extraction. Int. J. Heat Mass Tran. 92, 1205–1217. https://doi.org/10.1016/j.ijheatmasstransfer.2015.09.081.
Carcione, J.M., Poletto, F., Farina, B., Bellezza, C., 2018. 3D seismic modeling in geothermal reservoirs with a distribution of steam patch sizes, permeabilities and saturations, including ductility of the rock frame. Phys. Earth Planet. In. 279, 67–78. https://doi.org/10.1016/j.pepi.2018.03.004.
Carcione, J.M., Cavallini, F., Wang, E.J., Ba, J., Fu, L.Y., 2019. Physics and simulation of wave propagation in linear thermo-poroelastic media. JGR: Solid Earth 124, 8147–8166. https://doi.org/10.1029/2019JB017851.
Carcione, J.M., Farina, B., Poletto, F., Qadrouh, A.N., Cheng, W., 2020. Seismic attenuation in partially molten rocks. Phys. Earth Planet. In. 309, 106568 https://doi.org/10.1016/j.pepi.2020.106568.
Cui, X., Wong, L.N.Y., 2021. A 3D thermo-hydro-mechanical coupling model for enhanced geothermal systems. Int. J. Rock Mech. Min. Sci. 143, 104744 https://doi.org/10.1016/j.ijrmms.2021.104744.
Fawad, M., Hansen, J.A., Mondol, N.H., 2020. Seismic-fluid detection-a review. Earth Sci. Rev. 210, 103347 https://doi.org/10.1016/j.earscirev.2020.103347.
Fu, L.Y., 2019. Geophysical characterization of Olkaria geothermal reservoirs in Kenya. In: Tech. Report, BGPYJY2017-963. CNPC Greatwall Drilling Engineering Company Ltd.
Guitton, W.T., 2020. The value of geophysical data for geothermal exploration: examples from empirical, field, and synthetic data. Lead. Edge 39 (12), 864–872. https://doi.org/10.1190/tle39120864.1.
Guo, H., Thurber, C., 2022. Temporal changes in seismic velocity and attenuation at the geysers geothermal field, California, from double-difference tomography. JGR: Solid Earth 127, e2021JB022938. https://doi.org/10.1029/2021JB022938.
Heap, M.J., Reuschlé, T., Farquharson, J.I., Baud, P., 2018. Permeability of volcanic rocks to gas and water. J. Volcanol. Geoth. Res. 354, 29–38.
Hou, W.T., Fu, L.Y., Carcione, J.M., Wang, Z.W., Wei, J., 2021. Simulation of thermoelastic waves based on the Lord-Shulman theory. Geophysics 86, T155–T164. https://doi.org/10.1190/geo2020-0515.1.
Hou, W.T., Fu, L.Y., Carcione, J.M., Han, T.C., 2022a. Reflection and transmission of plane waves in thermoelastic media. Front. Earth Sci. 10, 1–16. https://doi.org/10.3389/feart.2022.850331.
Hou, W.T., Fu, L.Y., Carcione, J.M., 2022b. Reflection and transmission of thermoelastic waves in multilayered media. Geophysics 87, MR117–MR128. https://doi.org/10.1190/geo2021-0542.1.
Hou, W.T., Fu, L.Y., Carcione, J.M., 2023. Amplitude-variation-with-offset in thermoelastic media. Geophysics 88 (1), MR25–MR33. https://doi.org/10.1190/geo2021-0815.1.
Ignaczak, J., Ostoja, S.M., 2010. Thermoelasticity with Finite Wave Speeds. Oxford University Press.
Karingithi, C.W., Arnórsson, S., Grönvold, K., 2010. Processes controlling aquifer fluid compositions in the Olkaria geothermal system, Kenya. J. Volcanol. 196, 57–76. https://doi.org/10.1016/j.jvolgeores.2010.07.008.
Lasheen, E.S.R., Rashwan, M.A., Azer, M.K., 2023. Effect of mineralogical variations on physico-mechanical and thermal properties of granitic rocks. Sci. Rep. 13, 10320 https://doi.org/10.1038/s41598-023-36459-9.
Lemmon, E.W., McLinden, M.O., Friend, D.G., 2005. Thermophysical properties of fluid systems. In: Lindstrom, P.J., Mallard, W.G. (Eds.), NIST Chemistry Webbook 69. NIST Standard Reference Database.
Li, N.Q., Deng, W.B., Fu, L.Y., Carcione, J.M., Han, T.C., 2022. Wave propagation in double-porosity thermoelastic media. Geophysics 87 (6), MR265–MR277. https://doi.org/10.1190/geo2022-0008.1.
Li, N.Q., Fu, L.Y., Deng, W.B., Carcione, J.M., Yang, J., 2023. A thermo-hydro-mechanical model to evaluate the seismic properties of geothermal reservoirs. Geophysics 88 (5), WB23–WB35. https://doi.org/10.1190/geo2022-0491.1.
Liu, F., Fu, P.C., Mellors, R.J., Plummer, M.A., Ali, S.T., Reinisch, E.C., Liu, Q., Feigl, K.L., 2018. Inferring geothermal reservoir processes at the raft river geothermal field, Idaho, USA, through modeling InSAR-measured surface deformation. JGR: Solid Earth 123 (5), 3645–3666. https://doi.org/10.1029/2017JB015223.
Lord, H.W., Shulman, Y., 1967. A generalized dynamical theory of thermoelasticity. J. Mech. Phys. Solid. 15, 299–309. https://doi.org/10.1016/0022-5096(67)90024-5.
Lu, S.M., 2018. A global review of enhanced geothermal system (EGS). Renew. Sustain. Energy Rev. 81, 2902–2921. https://doi.org/10.1016/j.rser.2017.06.097.
Macdonald, R., Belkin, H.E., Fitton, J.G., et al., 2008. The roles of fractional crystallization, magma mixing, crystal mush remobilization and volatile-melt interactions in the genesis of a young basalt-peralkaline rhyolite suite, the greater OlkariaVolcanic complex, Kenya Rift Valley. J. Petrol. 49, 1515–1547. https://doi.org/10.1093/petrology/egn036.
Marshall, A.S., Macdonald, R., Rogers, N.W., et al., 2009. Fractionation of peralkaline silicic magmas: the greater olkaria volcanic complex, Kenya Rift Valley. J. Petrol. 50, 323–359. https://doi.org/10.1093/petrology/egp001.
Mwaura, D., Kada, M., 2017. Developing a web-based spatial decision support system for geothermal exploration at the Olkaria geothermal field. Int J Digit Earth 10 (11), 1118–1145. https://doi.org/10.1080/17538947.2017.1284909.
Noda, N., 1990. Thermal stress problem in a fluid-filled porous circular cylinder. Z. Angew. Math. Mech. 70, 543–549. https://doi.org/10.1002/zamm.19900701203.
Ofwona, C.O., 2002. A Reservoir Study of Olkaria East Geothermal System, Kenya. United Nations University, Geothermal Training Programme.
Omenda, P.A., 1998. The geology and structural controls of the Olkaria geothermal system. Kenya. Geothermics 27 (1), 55–74. https://doi.org/10.1016/S0375-6505(97)00028-X.
Pandey, S.N., Vishal, V., Chaudhuri, A., 2018. Geothermal reservoir modeling in a coupled thermo-hydro-mechanical-chemical approach: a review. Earth Sci. Rev. 185, 1157–1169. https://doi.org/10.1016/j.earscirev.2018.09.004.
Poletto, F., Farina, B., Carcione, J.M., 2018. Sensitivity of seismic properties to temperature variations in a geothermal reservoir. Geothermics 76, 149–163. https://doi.org/10.1016/j.geothermics.2018.07.001.
Qi, H., Ba, J., Müller, T.M., 2021. Temperature effect on the velocityporosity relationship in rocks. JGR: Solid Earth 126, 19–27. https://doi.org/10.1029/2019JB019317.
Rathnaweera, T.D., Wu, W., Ji, Y.L., Gamage, R.P., 2020. Understanding injection-induced seismicity in enhanced geothermal systems: from the coupled thermo-hydro-mechanical-chemical process to anthropogenic earthquake prediction. Earth Sci. Rev. 205, 103182 https://doi.org/10.1016/j.earscirev.2020.103182.
Rop, E., 2013. Interpretation of recent temperature and pressure data and updated conceptual model of greater olkaria geothermal systems, Kenya, north Iceland. UNU geothermal training program, reykjavik, Iceland. Report 32.
Rop, E., Hikari, F., Saeid, J., 2018. An updated numerical model of the Greater Olkaria geothermal system, Kenya. In: PROCEEDINGS, 43rd Workshop on Geothermal Reservoir Engineering Stanford University, Stanford, California, February 12-14, SGP-TR-213.
Salaun, N., Toubiana, H., Mitschler, J.B., Gigou, G., Carriere, X., Maurer, V., Richard, A., 2020. High-resolution 3D seismic imaging and refined velocity model building improve the image of a deep geothermal reservoir in the Upper Rhine Graben. Lead. Edge 39 (12), 857–863. https://doi.org/10.1190/tle39120857.1.
Shi, Y.Z., Rop, E., Wang, Z.C., Jiang, G.Z., Wang, S.J., Hu, S.B., 2021. Characteristics and formation mechanism of the Olkaria geothermal system, Kenya revealed by well temperature data. Geothermics 97, 1–12. https://doi.org/10.1016/j.geothermics.2021.102243.
Simiyu, S.M., 2000. Geothermal reservoir characterization: application of microseismicity and seismic wave properties at Olkaria, Kenya rift. JGR: Solid Earth 105 (B6), 13779–13795. https://doi.org/10.1029/1999JB900401.
Simiyu, S.M., Keller, G.R., 2000. Seismic monitoring of the olkaria geothermal area, Kenya Rift valley. J. Volcanol. Geoth. Res. 95 (1–4), 197–208. https://doi.org/10.1016/S0377-0273(99)00124-9.
Simiyu, S.M., Keller, G.R., 2001. An integrated geophysical analysis of the upper crust of the southern Kenya rift. Geophys. J. Int. 147 (3), 543–561. https://doi.org/10.1046/j.0956-540x.2001.01542.x.
Vidal, J., Genter, A., Chopin, F., 2017. Permeable fracture zones in the hard rocks of the geothermal reservoir at Rittershoffen, France. J. Geophys. Res. Solid Earth 122 (7), 4864–4887. https://doi.org/10.1002/2017JB014331.
Wang, P.J., Chen, C.Y., Zhang, Y., Go, Y.F., Qu, X.J., Yi, J., 2015. Characteristics of volcanic reservoirs and distribution rules of effective reservoirs in the Changling fault depression, Songliao Basin. Nat. Gas. Ind. 2 (12), 440–448. https://doi.org/10.1016/j.ngib.2015.09.020.
Wang, K., Yuan, B., Ji, G.M., Wu, X.R., 2018. A comprehensive review of geothermal energy extraction and utilization in oilfields. J. Pet. Sci. Eng. 168, 465–477. https://doi.org/10.1016/j.petrol.2018.05.012.
Wang, Z.W., Fu, L.Y., Wei, J., Hou, W.T., Ba, J., Carcione, J.M., 2020. On the Green function of the Lord–Shulman thermoelasticity equations. Geophys. J. Int. 220, 393–403. https://doi.org/10.1093/gji/ggz453.
Wang, E., Carcione, J.M., Yuan, Y., Ba, J., 2021. Reflection of inhomogeneous plane waves at the surface of a thermo-poroelastic medium. Geophys. J. Int. 224 (3), 1621–1639. https://doi.org/10.1093/gji/ggaa543.
Wei, J., Fu, L.Y., Wang, Z.W., Ba, J., Carcione, J.M., 2020. Green's function of the Lord–Shulman thermo-poroelasticity theory. Geophys. J. Int. 221 (3), 1765–1776. https://doi.org/10.1093/gji/ggaa100.
Wei, Y.J., Ba, J., Carcione, J.M., Fu, L.Y., Pang, M.Q., Qi, H., 2021. Temperature, differential pressure, and porosity inversion for ultradeep carbonate reservoirs based on 3D rock-physics templates. Geophysics 86 (3), M77–M89. https://doi.org/10.1190/geo2020-0550.1.
West, J.E.C., 2009. The Olkaria Optimization Study (Phase II)–Final Reservoir Analysis Report. West Japan Engineering Consultants. Inc.
Whitman, C., Iddings, J.P., Pirsson, L.V., Washington, H.S., 1902. A quantitative chemico mineralogical classification and nomenclature of igneous rocks. J. Geol. 10 (6), 555–690. https://doi.org/10.1086/621030.

Yang, J., Fu, L.Y., Fu, B.Y., Wang, Z.W., Hou, W.T., 2021. High-temperature effect on the material constants and elastic moduli for solid rocks. J. Geophys. Eng. 18 (4), 583–593. https://doi.org/10.1093/jge/gxab037.

Zhang, Z.M., Wei, X.D., Yang, H.T., Hu, S.B., Wang, Z.W., Shi, Y.Z., 2018. Characteristics of Olkaria Geothermal Field, a rift volcanic geothermal system. Sino-Global Energy 23 (12), 16–21. https://doi.org/10.6038/cjg2021N0458 (in Chinese).

Zhao, G.K., Hu, Y.Q., Jin, P.H., Hu, Y.F., Li, C., Zhu, X.Z., 2019. Experimental study on mechanical properties of granite subjected to cyclic loads under real time temperature. CJRME 38 (12), 927–937. https://doi.org/10.13722/j.cnki.jrme.2018.1277.